Radio Science®

RESEARCH ARTICLE

Key Points:

- Orbital Angular Momentum of radio waves can be used to improve precision pointing
- Low-sidelobe vortex beams can be seen as difference patterns of monopulse radars
- Exploiting at best Convex Programming and Singular Value Decomposition allows outperforming classical synthesis techniques

Correspondence to:

A. F. Morabito,
andrea.morabito@unirc.it

Author Contributions:

Conceptualization: Giada M. Battaglia, Tommaso Isernia, Roberta Palmeri, Andrea F. Morabito
Methodology: Giada M. Battaglia, Tommaso Isernia, Roberta Palmeri, Andrea F. Morabito
Software: Giada M. Battaglia, Tommaso Isernia, Roberta Palmeri, Andrea F. Morabito
Validation: Giada M. Battaglia, Tommaso Isernia, Roberta Palmeri, Andrea F. Morabito
Writing – original draft: Giada M. Battaglia, Tommaso Isernia, Roberta Palmeri, Andrea F. Morabito
Writing – review & editing: Giada M. Battaglia, Tommaso Isernia, Roberta Palmeri, Andrea F. Morabito

Synthesis of Orbital Angular Momentum Antennas for Target Localization

Giada M. Battaglia[1,2] ![ORCID], **Tommaso Isernia**[1,2] ![ORCID], **Roberta Palmeri**[1,2,3], and **Andrea F. Morabito**[1,2] ![ORCID]

[1]DIIES Department, Università Mediterranea di Reggio Calabria, Reggio Calabria, Italy, [2]Consorzio Nazionale Interuniversitario per le Telecomunicazioni (CNIT), Parma, Italy, [3]Institute for the Electromagnetic Sensing of the Environment of the National Council of Research (IREA-CNR), Napoli, Italy

Abstract The exploitation of Orbital Angular Momentum (OAM) is proposed to design circular-support continuous aperture distributions and concentric-ring arrays for target-localization applications. The proposed approach allows generating a single isolated null of the field in the target direction, which is of interest with respect to common techniques leading to a line (or perpendicular lines) of power-pattern zeroes in the spectral plane. In the presented design procedure, the optimal continuous aperture source is first identified by resorting to the most suitable OAM vortex and effective tools such as the Singular Value Decomposition of the involved operator and a smart Convex Programming optimization. Then, by exploiting fast deterministic algorithms, this continuous source is discretized into circular-ring arrays emulating it at best. Relevant applications including equispaced arrays, sum-difference reconfigurable arrays, and isophoric sparse arrays are presented. The proposed approach is also compared with the state-of-the-art techniques and assessed through full-wave electromagnetic simulations.

Plain Language Summary The addressed problem is the synthesis of power patterns for target localization. The present work provides an original and relevant contribution to the research community by introducing a new method to design circularly-symmetric continuous aperture distributions as well as circular-ring arrays able to maximize the localization accuracy while keeping under control both the beamwidth and the sidelobe level of the power pattern. By virtue of the powerful tools that are jointly exploited, which include the Orbital Angular Momentum beam modes, the Singular Value Decomposition of the corresponding operator, and a Convex Programming optimization of the problem's unknowns, the proposed approach results deeply different from those available in the literature and can overcome a number of intrinsic limitations of the latter. Hence, the achieved results are relevant and original from both the methodological and application points of view. With respect to the available solutions, the introduced paradigm will provide a number of advantages in terms of both application range and technological impact.

1. Introduction

Target localization applications take advantage of "difference" (Δ) or "delta-square" (Δ-square) patterns to localize targets, and the relevance of the subject is witnessed by the interest in classical design approaches (Bayliss, 1968; Bucci et al., 2005; Elliott, 1976; McNamara, 1993) as well as by the large number of more recent contributions such as for example (Fan et al., 2020, 2022; M. Li et al., 2021; Morabito et al., 2010; Palmeri et al., 2018; Qi & Li, 2021).

In a nutshell, in the receive mode one aims to have a null (with the steepest slope) at boresight while fulfilling upper-bound constraints on the sidelobes. In fact, the presence of the null allows for better localization performance with respect to directive patterns pointing at the target direction (Bucci et al., 2005; McNamara, 1993).

Usually, planar antennas generating difference patterns exhibit an antisymmetric behavior resulting in a whole line of field zeroes in the spectral plane (or two perpendicular rows of zeroes in the case of delta-square patterns) (Bucci et al., 2005; Fan et al., 2020). Therefore, while requiring a simple beamforming network and providing an easy commutation between the sum and difference modes, these systems may imply ambiguities and hence loss of resolution in the azimuth direction when the Δ-pattern comes from elevation (and vice-versa). Moreover, until the target direction has been found by using both the orthogonal Δ-patterns, the slope along the localization direction at hand depends on the expression of the pattern along the orthogonal direction. In fact, one has different slopes along the "null line" in the orthogonal direction.

Hence, it makes sense to look for other kinds of patterns devoted to the receive mode. To this end, OAM beams are of interest. In fact, OAM vortices can be used to generate fields having a single isolated null at boresight while avoiding, at the same time, lines of zeroes (through boresight) over the spectral plane (Morabito et al., 2018). With respect to traditional Δ patterns, this kind of fields may induce an increase of the time required in order to locate the target (since it cannot measure the azimuth or elevation angle independently, through 1-D scanning), but it may also significantly increase the localization accuracy. Such possible upgrading, together with the advantages listed in Section 3, is one of the reasons why OAM antennas have attracted growing attention in radar detection (Chen et al., 2020; Kou & Yu, 2022; Lin et al., 2016; Yu & Kou, 2023; Zhang & Chen, 2017; Zhang et al., 2019).

Obviously, the problem then arises of how many (and which) OAM vortices have to be used, and how to keep under control the sidelobe level (SLL) (Kou & Yu, 2022; Liu et al., 2016; Yin et al., 2014; Yu & Kou, 2023; Zhu et al., 2022), which also affects the overall localization performance.

In order to give a contribution to the solution of the above problem, we propose herein a novel OAM-based synthesis procedure for circularly-symmetric power patterns whose azimuth cuts are Δ beams maximizing the boresight slope while granting full control of both the beamwidth and the SLL over the whole spectral plane. In the developed procedure, "ideal" continuous aperture sources are first synthesized by using a Convex Programming (CP) algorithm that, in turn, relies on a field expansion making the best possible use of the OAM beam properties. Then, these continuous distributions are properly discretized into circular-ring arrays providing localization performances as close as possible to the ideal ones.

In the following, we provide in Section 2 a mathematical background on the OAM beam properties exploited by the proposed approach. Then, in Section 3 we outline the devised synthesis procedure. Finally, in Section 4 we present interesting applications of the proposed approach to the synthesis of array antennas having different architectures, and we also include full-wave electromagnetic simulations as well as comparisons with the most recent techniques available for the design of concentric annulus arrays devoted to low sidelobe vortex wave generation. Conclusion follows.

2. Background on OAM Beam Properties

The proposed approach exploits the expansions reported by Morabito et al. (2018) for representing the sought (circular-support) continuous aperture source and its spectrum. For the sake of self-consistency, these latter are briefly recalled in the following.

By denoting with (k, ϕ) and (ρ', ϕ') the radial and azimuth coordinates respectively spanning the spectral and aperture planes, the far-field pattern and the corresponding continuous aperture distribution can be respectively expanded in terms of the ℓ-order OAM modes $f_\ell(\rho')$ and $F_\ell(k)$ as follows:

$$F(k, \phi) = \sum_{\ell=-\infty}^{+\infty} F_\ell(k) e^{j\ell\phi} \tag{1a}$$

$$f(\rho', \phi') = \sum_{\ell=-\infty}^{+\infty} f_\ell(\rho') e^{j\ell\phi'} \tag{1b}$$

where proper truncations can be performed by following the rules in Palmeri et al. (2022), while the following relationship between $f_\ell(\rho')$ and $F_\ell(k)$ holds true:

$$F_\ell(k) = \int_0^a f_\ell(\rho') J_\ell(k\rho') \rho' d\rho' = H_\ell\{f_\ell(\rho')\} \tag{2}$$

a, $J_\ell(\cdot)$, and $H_\ell(\cdot)$ respectively denoting the aperture radius, the ℓ-th order Bessel function of the first kind, and the ℓ-th order Hankel transform (Bracewell, 1999; Piessens, 2000), supposing $f_\ell(\rho') = 0$ for $\rho' > a$. Therefore, the ℓ-th OAM spectrum mode $F_\ell(k)$ is equal to the ℓ-th order Hankel transform of the corresponding OAM source mode $f_\ell(\rho')$. This relation holds true for any aperture antenna having a finite circular support. In fact, whatever the electromagnetic source, the field distribution which is realized near the antenna surface will generate the actual radiation pattern by always obeying Equation 2 (or an equivalent Fourier Transform, if the antenna aperture is not circular).

It is worth noting that, by following the rules reported in Morabito et al. (2018) and Palmeri et al. (2022), Equation 2 can be rewritten in an operator form, that is,

$$F_\ell = A_\ell f_\ell \tag{3}$$

and, then, the Singular Value Decomposition (SVD) of A_ℓ can be performed. Hence, denoting with $u_{\ell,n}$ the resulting n-th right-hand singular function associated with the ℓ-th order, each OAM spectrum mode can be expanded as follows (Palmeri et al., 2022):

$$F_\ell(k) = \sum_{n=1}^{N_\ell} b_{\ell,n} u_{\ell,n}(k) \tag{4a}$$

with

$$N_\ell = \frac{2a}{\lambda} - \frac{|\ell|}{\pi} \tag{4b}$$

$\{b_{\ell,n}\}$ being suitable coefficients.

Coming back to Equation 2, it is clear that $\forall \ell \neq 0$ the function $J_\ell(\cdot)$ inside its kernel exhibits a $|\ell|$-th order zero in the origin. Therefore, $\forall \ell \neq 0$ and whatever the source, the OAM far-field modes exhibit a null with increasing order (and hence with a smoother behavior around the origin) for increasing values of $|\ell|$ in the boresight direction, while still being different from zero elsewhere. This property suggests the opportunity of exploiting OAM beams for the synthesis of difference patterns, which is one of the key features of the synthesis approach we are going to present.

The fact that OAM beams can be seen as a type of difference patterns of monopulse radars has been already exploited by the synthesis techniques recently published in Kou and Yu (2022) and Yu and Kou (2023). In this paper, we make some steps forward, as we identify further useful properties and introduce a new procedure exploiting (1)–(4) in such a way to allow a better (and joint) control of the power pattern boresight slope, beamwidth, and SLL.

The rationale and details of the devised synthesis technique are given in the next Section.

3. The Synthesis Approach

The aim of the proposed approach is to generate a circularly-symmetric Δ power pattern exploiting at best the potentialities of OAM modes and allowing the maximization of the boresight slope as well as the full control of the beamwidth and the SLL. This goal is achieved through the following steps:

(i) identify an "ideal", circularly-symmetric continuous aperture distribution able to achieve the best theoretical performances;

(ii) discretize the ideal continuous distribution into a circular-ring array emulating it.

Notably, once the optimal continuous source has been identified, step (ii) can be performed by adapting to the present case equations or algorithms that have been previously developed. Therefore, the discussion of this step is postponed to the following Section, where the discretization of the reference continuous distribution will be separately outlined by presenting different array-design applications as well as comparisons with the techniques proposed in Kou and Yu (2022) and Yu and Kou (2023).

As far as step (i) is concerned, it is performed by taking into account the fact that, in order to generate a circularly-symmetric power pattern, the spectrum must be composed of a single OAM vortex. In fact, if the spectrum is conceived as a superposition of OAM beams having different orders, these latter will interfere in a different fashion for different values of ϕ, thus resulting in the loss of the circular symmetry of $|F|$. Therefore, the synthesis of the continuous aperture distribution is carried out through the three following steps:

(i.1) the most suitable OAM vortex order, say $\hat{\ell}$, is identified;

(i.2) the SVD of $A_{\hat{\ell}}$ is computed. Then, the difference pattern is set as the $\hat{\ell}$-th order OAM spectrum mode and it is expanded as in Equations 4a and 4b, that is,

$$F_{\hat{\ell}}(k) = \sum_{n=1}^{N_{\hat{\ell}}} b_{\hat{\ell},n} u_{\hat{\ell},n}(k) \tag{5}$$

Finally, a CP optimization is performed in the unknowns $\{b_{\hat{\ell},n}\}$ in such a way to enforce the desired radiation requirements in terms of SLL, beamwidth, and boresight slope;

(i.3) the continuous aperture distribution is determined as:

$$f_{\hat{\ell}}(\rho') = \sum_{n=1}^{N_{\hat{\ell}}} a_{\hat{\ell},n} v_{\hat{\ell},n}(k) \tag{6}$$

where $a_{\hat{\ell},n} = b_{\hat{\ell},n}/\sigma_{\hat{\ell},n}$, $\sigma_{\hat{\ell},n}$, and $v_{\hat{\ell},n}$ respectively being the nth singular value and nth left-hand singular function coming out from the SVD of $A_{\hat{\ell}}$.

Alternatively, supposing the amplitude of the synthesized spectrum is sufficiently small at the border of the visible range and beyond, the aperture distribution can be identified through either the inverse Fourier transform of $F(k, \phi)$ or the following inverse Hankel transform:

$$f_{\hat{\ell}}(\rho') = H_{\hat{\ell}}^{-1}\{F_{\hat{\ell}}(k)\} \tag{7}$$

As far as step (i.1) is concerned, an obvious brute-force strategy would be to repeatedly execute step (i.2) for different values of $\hat{\ell}$ and, then, a-posteriori pick the OAM vortex order leading to largest boresight slope. However, by means of a deeper understanding, one does not need here any trial-and-error procedure, as the optimal order can be identified by exploiting the following criteria:

(a) even-order OAM beams (including the 0-th order one) must be avoided since they induce a field slope equal to zero at boresight;

(b) since the larger the value of $|\ell|$ the larger the width of the boresight null, $|\hat{\ell}| = 1$ is the choice guaranteeing the maximization of the power pattern's slope in the target direction (and hence the maximization of the target-localization resolution).

By virtue of the statements (a)-(b), $F_{\pm1}(k)$ can be safely selected as the optimal solution of step (i.1).

Once $\hat{\ell}$ has been identified and the variable k has been properly discretized, that is, $k = [k_1, k_2, \dots, k_M]$ (with $k_1 = 0$ and $k_M = \beta = 2\pi/\lambda$, β and λ respectively denoting the wavenumber and the operating wavelength), the SVD of $A_{\hat{\ell}}$ can be computed and $F_{\hat{\ell}}(k)$ can be expanded as in (5). Then, by paralleling (Bucci et al., 2005) and considering the boresight as the target direction, step (i.2) can be completed by solving, in the unknowns $\{b_{\hat{\ell},n}\}$, the following CP optimization problem:

$$\min_{b_{\hat{\ell},n}}\left\{-Re\left[\frac{F_{\hat{\ell}}(k_2) - F_{\hat{\ell}}(k_1)}{k_2 - k_1}\right]\right\} \tag{8}$$

subject to:

$$Im\left[\frac{F_{\hat{\ell}}(k_2) - F_{\hat{\ell}}(k_1)}{k_2 - k_1}\right] = 0 \tag{9}$$

$$|F_{\hat{\ell}}(k)|^2 \leq UB(k) \quad \forall k \in \Omega \tag{10}$$

where Re and Im respectively denote the real and imaginary parts, while UB is an upper-bound function allowing the full control of both the beamwidth and the SLL inside the Ω region. Obviously, by enforcing suitable linear phases over the aperture distribution, beam scanning can also be performed.

As far as the discretization of k is concerned, using a sampling rate larger than the Nyquist one given in Bucci et al. (1998) is recommended. In the following, we assume $M = \lceil 10 \times 2a/\lambda \rceil$.

Interestingly, minimization (8) subject to the constraint (9) is equivalent to maximizing the "discretized" slope at boresight (and hence the accuracy of the target localization), while fulfillment of the constraint (10) allows, at the same time, to enforce an arbitrary upper bound on the peak sidelobe level (and hence to fully control the SLL over the whole visible range).

Notably, the overall optimization consists in minimizing a linear function of the unknowns in the convex set that is given by the intersection of the linear equality (9) and the quadratic inequality (10). As such, it is a CP problem where the global optimum is unique and the fast identification of the solution is guaranteed. By virtue of this circumstance, the solution procedure is expected to be more effective than all the techniques aimed at keeping under control the SLL of OAM beams by recurring to global optimization algorithms—see for instance (Qin et al., 2017; Q. Li et al., 2018, 2019).

Finally, once the coefficients $\{b_{\hat{\ell},n}\}$ have been identified, step (i.3) can be readily performed by computing the aperture source through (6) or (7).

As outlined above, in the subsequent step (ii) of the overall procedure, this distribution will be used both as a reference and benchmark in order to design circular-ring arrays as well as to understand the ultimate theoretical performances achievable for the given aperture size (see Section 4).

As far as the relationship and comparison of the proposed OAM beam with the traditional difference pattern, the following comments are in order. While the traditional difference beams (where one needs two operating modes and some switching) can quickly determine the azimuth and elevation angle of the target through a couple of one-dimensional scans, the presented "single-pattern" technique does not allow measuring the azimuth or elevation angle independently, which may increase the time for locating the target, as a planar scanning of the spectral domain would be required. On the other side, the proposed solution still has a number of attractive characteristics as follows:

- if switching or Digital Signal Processing is required, one can jointly use the traditional difference patterns and the OAM optimal pattern to get, respectively, an initial estimation (from the first couple) and a faster steering chase (from the OAM operating mode);
- if a purely hardware solution is looked for, avoiding the switch after the target has been hooked can be of interest;
- in a number of applications, such as for instance precision pointing or airborne missile guidance systems (Bleakney, 1984; Kennedy et al., 1995), one approximately knows the target direction, so that just a small portion of the space must be explored.

A further relevant question concerns the quantitative performance of the proposed method as compared to traditional difference patterns, which should be measured in terms of the slope. As far as one reasons, by the sake of simplicity, on the case of traditional solutions with factorable patterns, the slope of the null (and hence the localization precision along the direction at hand) is not univocally determined unless the pattern along the orthogonal direction is constant. In fact, it may also be a null slope (if one has a null in the pattern along the orthogonal direction). Note this is not the case with the proposed solution, where the slope is uniquely determined. Obviously, in the traditional solutions one can redetermine a kind of optimal slope by subsequent iterative adjustments of the linear phases of the array excitations along both directions, but this is not anymore a "two-scans-only" situation. Moreover, and more importantly, the slope along the two main directions depends on the size of the source along its sides, so that it may be very different from the one pertaining to the optimal OAM configuration.

These circumstances are some of the reasons why OAM antennas are becoming more and more useful in target-localization applications (Chen et al., 2020; Kou & Yu, 2022; Lin et al., 2016; Liu et al., 2016; Yin et al., 2014; Yu & Kou, 2023; Zhang & Chen, 2017; Zhang et al., 2019; Zhu et al., 2022). As far as comparisons with some of these contributions are concerned, the proposed technique is actually meant to "remove" some important limitations of the state-of-the-art OAM-based radars and to increase their performance in terms of localization accuracy. Furthermore, as shown in the following Section, the proposed technique allows, for equal source size and far-field beamwidth and slope, better control of the sidelobe level and hence the capability to work more efficiently in realistic complex environments where electromagnetic interference is present.

4. Applications Plus Comparison With the State-Of-The-Art Techniques

In order to validate the proposed approach, we present in this Section different applications as follows.

First, in Section 4.1, we provide a numerical analysis aimed at understanding the impact of step (i.1), that is, the adopted vortex order, on the performance achievable at the end of step (i.2).

Table 1
Comparison of the Boresight Slope of the Power Patterns Shown in Figure 1a

$\hat{\ell}$	SLOPE (dB)
1	5.68
3	−25.24
5	−50.54

Then, applications involving different ways of discretizing the continuous aperture distributions are investigated. In particular, in Section 4.2, we compare the proposed approach with the techniques recently published by Kou and Yu (2022) and Yu and Kou (2023) for the synthesis of equispaced circular-ring arrays. Then, in Section 4.3, we address the design of an isophoric sparse ring array (which is then also full-wave simulated in Section 4.5). Finally, in Section 4.4, an ulterior continuous aperture source is synthesized and then exploited to design a "reconfigurable" equispaced circular-ring array able to generate sum and difference patterns for target-localization applications.

In order to show the achieved results, all array layouts and continuous aperture distributions are plotted with respect to the variables $x = \rho' \cos \phi'$ and $y = \rho' \sin \phi'$ while all power patterns are plotted with respect to the variables $k = \beta \sin \theta$, $u = k \cos \phi$, and $v = k \sin \phi$ (with $\rho' \in [0,a]$ and θ denoting the elevation angle from boresight).

All numerical experiments have been performed by setting the target direction as $\theta = 0°$. Furthermore, all results [but for the ones pertaining to the electromagnetic full-wave simulations and the comparison with Yu and Kou (2023)] have been generated without specifying any working frequency, that is, the aperture size has been expressed as a function of the generic wavelength λ so that all power patterns remain unchanged at any frequency. Finally, from now on, the SLL is meant as the difference between the maximum amplitude of the sidelobes and the maximum amplitude of the main beam of the power pattern.

4.1. Analyzing Performance With Different OAM Vortex Orders

By virtue of the properties (a)-(b) discussed in the previous Section, $\hat{\ell} = \pm 1$ always guarantees the best performance as it leads to fields having a null width smaller than any solutions achievable for any $|\hat{\ell}| > 1$. However, it makes sense to evaluate the maximum performance achievable by the presented technique when different vortex orders are exploited. To this end, we solved the problem (8)-(10) by enforcing the same *UB* mask while using different OAM vortex orders ranging from $\hat{\ell} = 1$ to $\hat{\ell} = 5$ [and exploiting only the odd orders by virtue of properties (a) and (b) reported in Section 3].

By setting $a = 5\lambda$ and $UB = 0$ dB for $\theta \geq 15°$, we achieved the results shown in Table 1 and Figure 1. In particular, Figure 1a shows the enforced *UB* mask as well as the superposition of the (circularly-symmetric) power patterns achieved for $\hat{\ell} = 1$, $\hat{\ell} = 3$, and $\hat{\ell} = 5$, while Figures 1b and 1c show the continuous aperture distribution corresponding to $\hat{\ell} = 1$. Moreover, Table 1 reports the boresight slope achieved in the three different test cases.

As it can be seen, for equal values of the three key parameters, that is, the aperture size, the maximum permitted amplitude of the sidelobes, and the main beam's null-to-null beamwidth, it is clear that the lowest $\hat{\ell}$ the largest
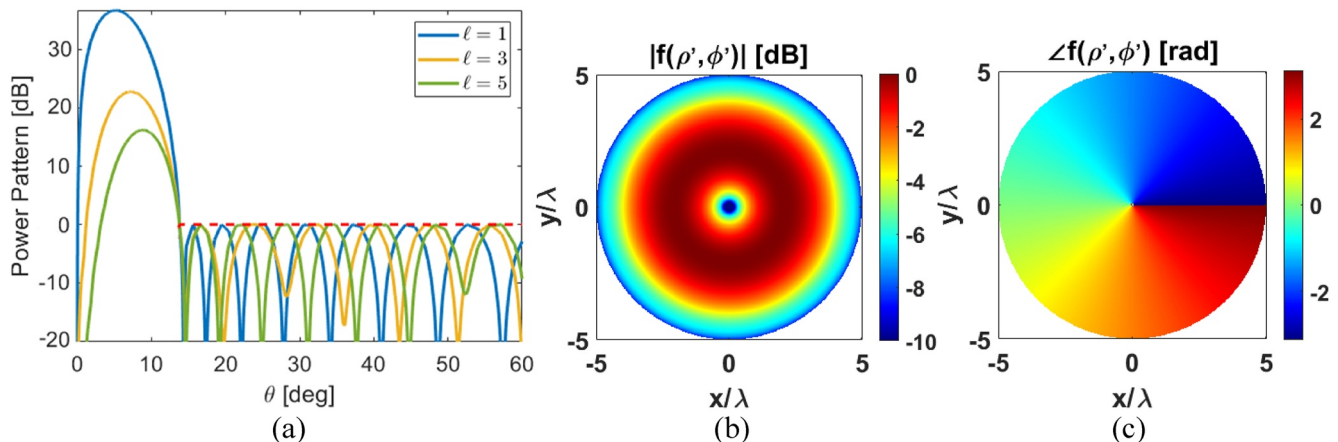

Figure 1. Verifying the best OAM mode: superposition between the *UB* function (red dashed curved) and the power patterns generated for different values of $\hat{\ell}$ [subplot (a)]; amplitude [subplot (b)] and phase [subplot (c)] of the continuous aperture distribution corresponding to the $\hat{\ell} = 1$ power pattern shown in subplot (a).
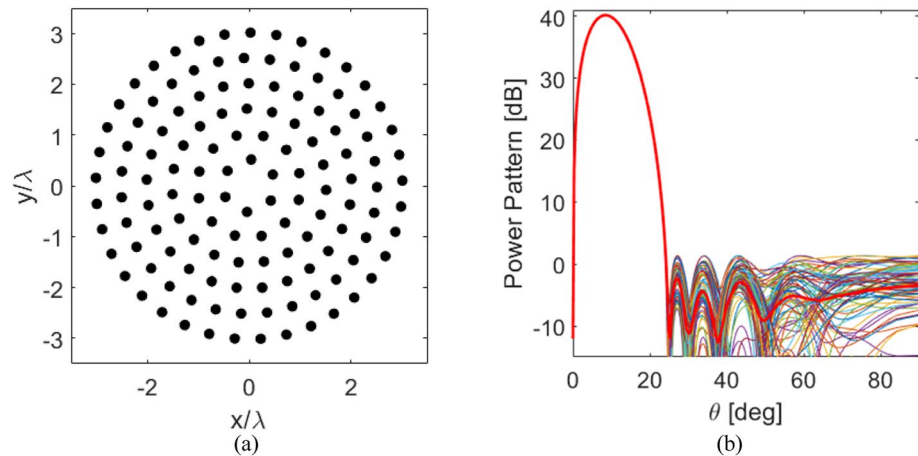
Figure 2. Comparison with Kou and Yu (2022): equispaced array composed of 131 isotropic elements [subplot (a)] and corresponding power pattern [subplot (b)]. All ϕ cuts of the power pattern are superimposed, and the average value is depicted in red.

the slope (and the lowest the value of θ at which the power pattern attains its maximum value). In particular, $\hat{\ell} = 1$ allows achieving a power-pattern slope that is not only (as expected) the "best" one, but also significantly better than the ones pertaining to the other OAM modes.

4.2. Equispaced Circular-Ring Arrays: Comparison With Kou and Yu (2022) and Yu and Kou (2023)

Notably, Kou and Yu (2022) and Yu and Kou (2023) are the most recent contributions addressing the synthesis of difference patterns through equispaced circular-ring arrays by exploiting OAM vortex beams. Given the high performance of the techniques presented therein, we thought it appropriate to compare the proposed approach with both of them.

As far as (Kou & Yu, 2022) is concerned, an effective design procedure has been devised pursuing the goal of minimizing the SLL by resorting to a modified Bayliss synthesis method. The best result has been achieved by using the $\ell = 1$ OAM vortex and a circular-ring array composed of 131 isotropic elements uniformly-located on 6 equispaced rings over a circular domain having a radius equal to 3λ. The spacing between consecutive rings as well as consecutive elements on each ring has been set as 0.5λ. The achieved power pattern is shown in Figure 4a of Kou and Yu (2022). Its maximum absolute value and its highest-amplitude sidelobe result respectively centered at $\theta = 8.5°$ and $\theta = 27.5°$. The minimization of the sidelobe level led to SLL = −36.44 dB.

To compare the proposed approach with the one in Kou and Yu (2022), we first synthesized a reference continuous source by solving the CP problem (8)-(10) using the same OAM vortex order and aperture size of Kou and Yu (2022), that is, $\hat{\ell} = 1$ and $a = 3\lambda$. We also set $UB = 0$ dB for $\theta \geq 26°$. Then, we generated the array layout shown in Figure 2a which shares with the one in Kou and Yu (2022) the isotropic element pattern as well as all key geometrical parameters, that is, the diameter, the number of rings, the inter-elements spacing, and the overall number of elements.

Since the synthesized continuous aperture distribution is not superdirective, as expected by virtue of the rules in Bucci et al. (2013), Hodges and Rahmat-Samii (1996), and Morabito et al. (2019) the small (half-a-wavelength) inter-element spacing of the array layout allowed identifying the optimal array excitations through a simple sampling operation. Hence, for each array element, the excitation has been identified as the value attained at its location by the reference continuous distribution. Finally, once the sampling of the continuous aperture distribution has been performed, the array excitation amplitudes have been further optimized by pursuing a fitting of the main lobe of the field radiated by the reference distribution while enforcing a constant upper bound on the sidelobes.

The power pattern generated by the synthesized array is shown Figure 2b. In such a figure, since the array geometry does not guarantee a circular symmetry of the final radiation pattern, a superposition of all ϕ cuts is shown. Moreover, the average power-pattern value is superimposed.

Table 2
Performance Parameters Comparison Between the Proposed Approach and the Best Result Reported in Kou and Yu (2022)

Performance parameters	Kou and Yu (2022)	This work
Index of the exploited OAM vortex	1	1
Aperture size	3λ	3λ
Array element pattern	Isotropic	Isotropic
Array number of elements	131	131
Coordinate of power pattern maximum absolute value	8.5°	8.5°
Coordinate of power pattern first sidelobe	27.5°	27.5°
Sidelobe level	−36.44 dB	−42.56 dB (average value)
		−38.81 dB (worst value)

Note. The presented technique allowed a significant improvement of the sidelobe level performance while keeping identical all the other design and radiation parameters.

Notably, while sharing with the best solution reported in Kou and Yu (2022) the coordinate of the power pattern's maximum absolute value (i.e., $\theta = 8.5°$) as well as the location of the first sidelobe (i.e., $\theta = 27.5°$), the achieved solution allowed a significant improvement of the SLL performance. In fact, despite the fact that an identical array has been used, the different ϕ cuts shown in Figure 2b have in the average a SLL equal to −42.56 dB, which is more than 6 dB lower than the one reported in Kou and Yu (2022). Even by considering the "worst" ϕ cut, that is, the one leading to the largest amplitude of sidelobes, the achieved solution provides a SLL equal to −38.81 dB and hence 2.37 dB lower than the one reported in Kou and Yu (2022). The comparison of all the key parameters is given in Table 2.

As far as (Yu & Kou, 2023) is concerned, it introduced a method for low sidelobe vortex beams synthesis by resorting to a Fourier-Bessel series expansion and concentric annulus arrays. As done in Kou and Yu (2022), by noting that OAM beams are similar to the difference patterns of monopulse radars, the Bayliss function has been exploited as the objective field. By so doing, as shown by Figure 7 of Yu and Kou (2023), it has been possible significantly outperform both the Dolph-Chebyshev and the Taylor synthesis methods.

The results achieved in Yu and Kou (2023) can be summarized as follows. At an operating frequency of 10 GHz, the concentric annulus array is composed of 822 isotropic radiating elements arranged on 15 rings having coordinates {24.5, 40.2, 55.5, 70.6, 85.8, 100.8, 115.9, 130.9, 146.0, 161.0, 176.0, 191.0, 206.0, 221.1, 236.1} (mm). The elements are evenly distributed over each ring with an arc length equal, in the outer rings, to 0.5λ (i.e., about 15 mm). This led to a number of antennas per ring equal to {10, 17, 23, 30, 36, 42, 49, 55, 61, 67, 74, 80, 86, 93, 99}. Finally, by using the $\ell = 2$ OAM vortex and an excitation amplitude per ring equal to {−1.78, −9.14, −4.01, −3.19, −0.73, −0.32, 0.00, −0.72, −1.54, −3.44, −5.64, −8.75, −11.78, −15.45, −18.61} dB, a difference beam with a peak SLL equal to −31.1 dB and a divergence angle equal to 5.3° has been achieved. This power pattern is shown in Figure 7 of Yu and Kou (2023) and, for the sake of clarity, it is reported also here (see figures below).

To test the proposed approach in this scenario, we adopted the same identical array layout, single-element pattern, and working frequency as the ones in Yu and Kou (2023). Furthermore, although our approach achieves the best results for $\hat{\ell} = 1$, we set $\hat{\ell} = 2$ as it was done in Yu and Kou (2023) in order to come to a perfectly fair comparison.

We synthesized the continuous reference source by using $a = 8\lambda$ and setting $UB = 0$ dB for $\theta \geq 12°$, and then we identified the array excitations by using the array layout shown in Figure 3a, which is identical to Figure 5 of Yu and Kou (2023).

As we did in our comparison with (Kou & Yu, 2022), we fed each array element by using the value attained at its location by the reference continuous distribution. This time, differently from the comparison with (Kou & Yu, 2022), no further optimization of the excitations has been performed. This procedure led to an excitation amplitude per ring equal to {−18.50, −10.72, −5.98, −2.49, −0.83, −0.04, 0.00, −0.63, −1.97, −3.96, −6.73, −10.34, −14.98, −21.12, −28.52} dB, which has been rounded by using the same significant digits as in Yu and Kou (2023) before computing the far field. As far as the elements' excitation phase is concerned, we used the same values as the ones exploited in Yu and Kou (2023) so that, in the end, the unique difference between the two numerical experiments is the elements' excitation amplitude.
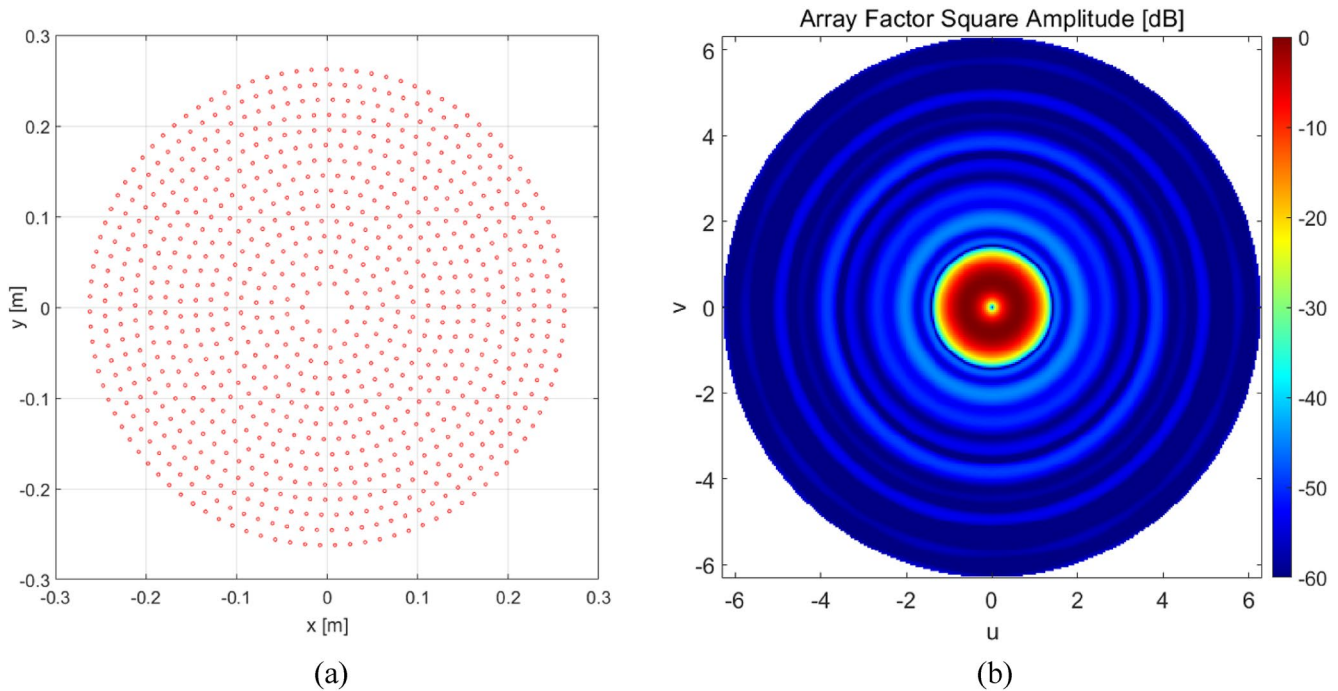
(a)   (b)

Figure 3. Comparison with Yu and Kou (2023): the adopted 822-elements array layout that is shown also in Figure 5 of Yu and Kou (2023) [subplot (a)] and the power pattern generated by means of our approach [subplot (b)].

The achieved power pattern is shown in Figure 3b in terms of the u and v spectral variables (as normalized with respect to $[-2\pi, +2\pi]$ range). Since it exhibits a circular symmetry, its performance can be easily analyzed by considering any of its φ cuts. Hence, in Figure 4 we superimposed the $\phi = 0°$ cuts of the power patterns respectively achieved by using the proposed approach and the technique in Yu and Kou (2023). As it can be seen, for an equal value of the divergence angle, and by adopting the same concentric annulus array as well as the same OAM vortex, our approach allowed to lower by more than 13 dB the peak SLL. In fact, while the divergence angle is equal to 5.3° for both patterns, our procedure leads to a peak SLL equal to −44.7 dB while the one in Yu and Kou (2023) grants a peak SLL equal to −31.1 dB. The comparison of all parameters is given in Table 3. The achieved results prove that, even if the choice of the vortex order is not optimized, the proposed approach is able to take the maximum possible advantage from OAM beams whatever the value of $\hat{\ell}$.
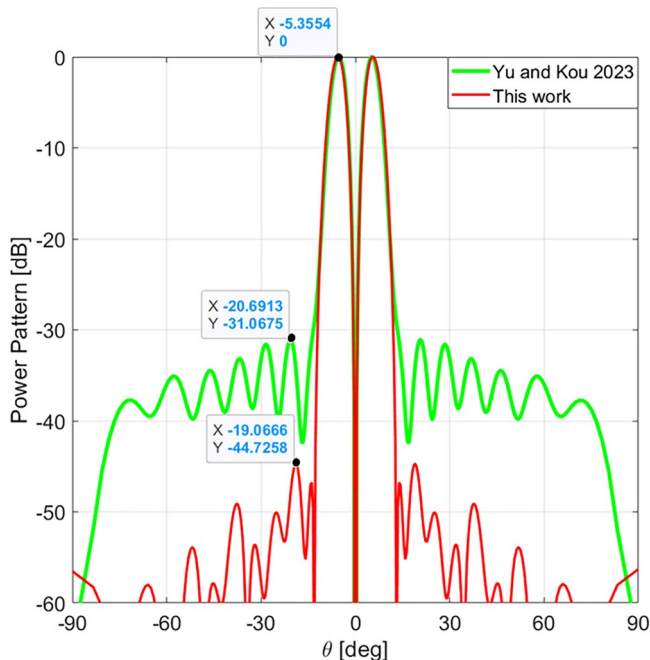

Figure 4. Superposition of the power patterns achieved by the array shown in Figure 3(a) when it is fed, respectively, by the excitations of Yu and Kou (2023) and the ones here synthesized.

4.3. Isophoric Sparse Arrays

In case a fixed simple receiving chain is in order, so that excitations' weighting is not allowed (but eventually for phase factors), it makes sense to look for arrays using positions (rather than excitation weights) to perform localization (Morabito et al., 2010).

By using as reference the continuous distribution shown in Figures 1b and 1c, we synthesized an "isophoric" array having a sparse layout and equal-amplitude excitations for all elements. As well known, this feature is also very convenient from the antenna fabrication point of view (Morabito & Nicolaci, 2018) since it allows a dramatic simplification of the beam forming network.
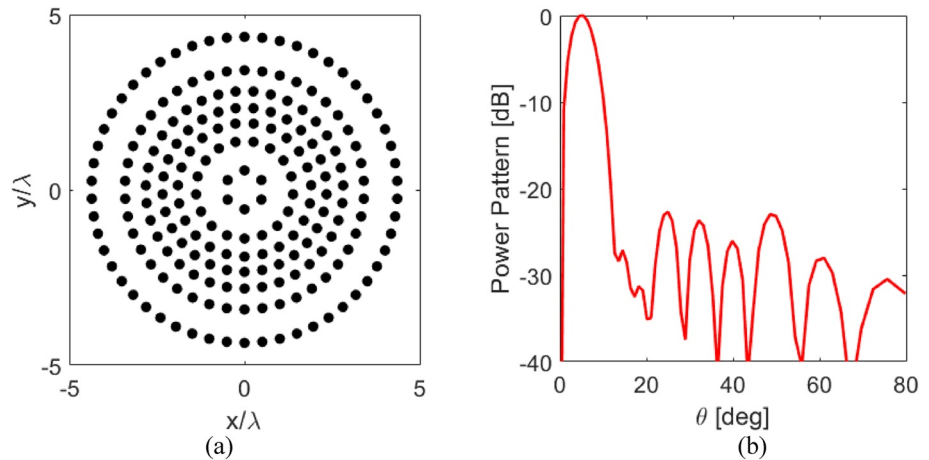
Figure 5. Isophoric sparse ring array layout designed through the steps (1)–(3) described in Section 4.3 [subplot (a)] and corresponding normalized power pattern [subplot (b)].

The array design has been performed by means of the following procedure:

(1) since the reference continuous distribution exhibits a constant phase distribution along the radial coordinate for each fixed value of ϕ' (see Figures 1b and 1c), we identified the array ring coordinates by applying the technique described in Bucci et al. (2013) to the amplitude of the $\phi' = 0$ cut of the continuous distribution. The achieved coordinate of the rings turned out to be equal to 0.55λ, 1.39λ, 1.90λ, 2.34λ, 2.82λ, 3.41λ, and 4.36λ;

(2) once the ring coordinates have been determined, we identified the elements' location on each ring by using a constant 0.5λ arc length spacing;

(3) we assigned to each element an excitation having a constant unitary amplitude and a phase equal to the phase attained by the reference continuous distribution at the element location.

The achieved array layout and the $\phi = 0°$ cut of the corresponding power pattern (exploiting, this time, a $\cos\theta$ element pattern) are respectively shown in Figures 5a and 5b. In particular, the array layout results composed of 206 elements which, as expected, are more densely located where the reference continuous distribution's amplitude is larger. It is worth noting that the adoption of a sparse array layout allowed saving roughly 30% of elements with respect to case where the elements' location is identified by performing a uniform 0.5λ sampling of the same reference continuous distribution (which would have led to a 287-elements equispaced layout).

The power pattern shown in Figure 5b attains its maximum absolute value at $\theta = 5.35°$ and results lowered by -28 dB at $\theta = 13°$. The SLL is equal to -22.7 dB. Since all excitations have the same, unitary amplitude, this configuration is also expected to dramatically reduce the weight, complexity, and cost of any possible related beam forming network (Morabito & Nicolaci, 2018).

4.4. Reconfigurable Arrays

As a further interesting application of the proposed approach, we synthesized a reconfigurable monopulse array for target-localization applications. In particular, the aim is to switch from a difference to a sum pattern (and vice versa) while sharing, between the two radiation modalities, the array layout as well as a high percentage of the array amplitude excitations.

In order to pursue the above goals, we first identified the optimal continuous distributions respectively corresponding to the two desired radiation modalities as reported below.

As far as the difference pattern is concerned, we kept the reference continuous distribution used in Subsections 4.1 and 4.3 and shown in Figures 1b

Table 3
Performance Parameters Comparison Between the Proposed Approach and the One in Yu and Kou (2023)

Performance parameters	Yu and Kou (2023)	This work
Index of the exploited OAM vortex	2	2
Array diameter	236.1 mm	236.1 mm
Array number of elements	822	822
Array element pattern	Isotropic	Isotropic
Operating frequency	10 GHz	10 GHz
Divergence angle	5.3°	5.3°
Peak sidelobe level	−31.1 dB	−44.7 dB

Note. The presented technique allowed a significant improvement of the sidelobe level by using the same array layout and OAM vortex order.

and 1c, say $f_\Delta(\rho', \phi')$. Due to the adopted field representation based on OAM modes, this distribution can be written as follows:

$$f_\Delta(\rho', \phi') = A_\Delta(\rho')e^{j\alpha_\Delta(\phi')} \tag{11}$$

denoting with A_Δ and α_Δ its amplitude and phase, respectively.

Then, we synthesized the reference continuous distribution for the sum pattern, say

$$f_\Sigma(\rho', \phi') = A_\Sigma(\rho')e^{j\alpha_\Sigma(\phi')} \tag{12}$$

by extending to the present case the theory reported in Morabito and Rocca (2010) (where it is also shown that the sources generating reconfigurable sum/difference patterns can have a very similar amplitude on the outer part of the aperture). In particular, since the optimal continuous source for a pencil beam with maximum directivity is expected to be real (Bucci et al., 2009), we set $\alpha_\Sigma = 0 \forall \phi'$ and then solved the following CP optimization problem in the (real) unknown $A_\Sigma(\rho')$:

$$\min_{A_\Sigma(\rho')} \left\{ \int_0^a A_\Sigma(\rho')^2 \rho' d\rho' \right\} \tag{13}$$

subject to:

$$A_\Sigma(\rho') \geq 0 \forall \rho' < R \tag{14}$$

$$A_\Sigma(\rho') = A_\Delta(\rho') \forall \rho' \geq R \tag{15}$$

$$|E_\Sigma(k)|^2 \leq U B_\Sigma(k) \forall k \geq K \tag{16}$$

denoting with $E_\Sigma(k)$ the far field for the sum radiation modality, that is,

$$E_\Sigma(k) = \int_0^a A_\Sigma(\rho') J_0(k\rho') \rho' d\rho' \tag{17}$$

In the above problem, the objective function in (13) represents the aperture power and, by virtue of the theory in Bucci et al. (2009), its minimization allows maximizing the directivity without incurring into superdirective solutions or fast-oscillating sources that would be difficult to be discretized. At the same time, the quadratic constraint (16) allows enforcing on the sidelobes an arbitrary upper-bound constraint $U B_\Sigma(k) \forall k \geq K$ (K being a parameter chosen by the user according to the particular radiation goals at hand). Finally, the linear constraints (14)–(15) lead to a positive aperture distribution which is equal, $\forall \rho' \geq R$, to the amplitude of the aperture distribution pertaining to the difference pattern.

We identified $A_\Sigma(\rho')$ [and hence $f_\Sigma(\rho', \phi')$] by using $UB = -20$ dB, $K = 1.1$, $a = 5\lambda$, and $R = 2.5\lambda$. Then, by following the procedure described in Subsection 4.2 (but using, this time, a 0.55λ elements spacing both between different rings as well as along the same ring), the distributions $f_\Sigma(\rho', \phi')$ and $f_\Delta(\rho', \phi')$ have been discretized into a uniformly-spaced circular-ring array. The resulting layout, which is fully shared by the two radiation modalities, is composed of 230 elements, and is shown in Figure 6a (which also reports, in its caption, the coordinate of the rings). Notably, in this figure, by virtue of constraint (15), the excitation amplitudes result equal for the sum and the difference patterns on the elements depicted in red. This means that switching between the two radiation modalities is performed by varying the excitation amplitude only on 30% of the elements.

The $\phi = 0°$ cut of the sum and difference square-amplitude far field distributions achieved by using a $\cos\theta$ element pattern are depicted in Figure 6b. The corresponding SLL results equal to -24 dB and -26 dB for the sum and the difference patterns, respectively. The difference pattern attains its maximum value at $\theta = 5.35°$ and results lowered by -28 dB at $\theta = 14.5°$. The null-to-null beamwidth of the sum pattern is given by $\theta = \pm 11.7°$.
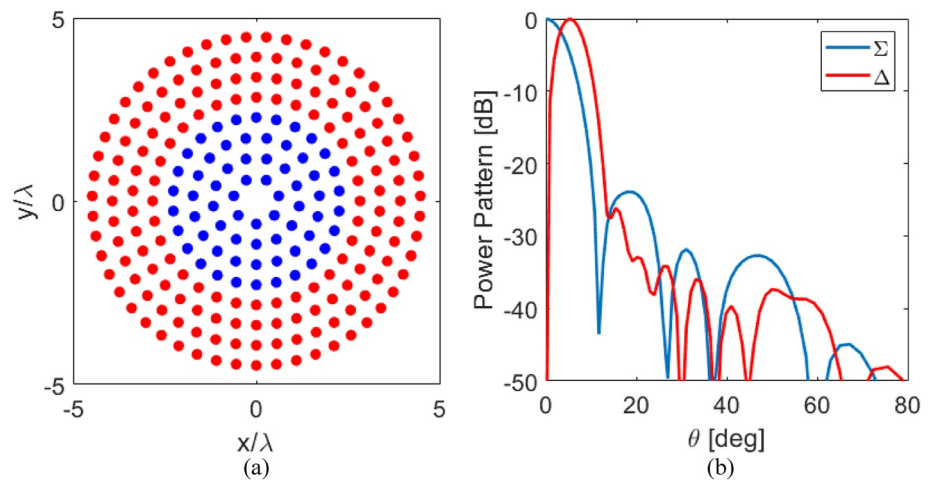
Figure 6. Reconfigurable array [subplot (a)] and corresponding sum and difference patterns [subplot (b)]. In the array layout, the red dots denote the elements whose excitation amplitude is shared between the sum and difference radiation modalities. Layout rings = [0.63λ 1.18λ 1.73λ 2.28λ 2.83λ 3.38λ 3.93λ 4.48λ].

As a final but of the utmost importance feature, the presented procedure also allows synthesizing a "phase-only" reconfigurable array (sharing 100% of the elements' excitation amplitudes for the two radiation modalities) by setting $R = 0$ when solving the optimization problem (13)-(16).

4.5. Full-Wave Electromagnetic Simulations

To definitively assess the presented technique in actual working conditions, we repeated the synthesis experiment described in Section 4.3 by performing a full-wave electromagnetic simulation through the CST Microwave Studio software (CST Studio Suite 3D EM simulation and analysis software, 2022).

Coming to details, we exploited as radiating element the realistic patch antenna shown in Figure 7. The overall design and optimization of this device have been performed by following the guidelines reported in Wei et al. (2015), where this antenna has also been fabricated in order to definitively assess its performance with the utmost reliability. The design parameters are reported in Table 4. Furthermore, by following the guidelines reported in Mekki et al. (2020), we performed a corner truncation which ensures the circular polarization of the antenna (see Figure 8a).

After having designed the single radiating element, we have reached the antenna layout shown in Figure 8 by using the circular-ring radii reported in Section 4.3 and slightly enhancing the inter-antenna angular distance inside each ring from 0.5λ to 0.55λ in order to minimize the mutual coupling effects. By virtue of this choice, the array layout results now composed of 187 elements and hence allows saving roughly 10% of elements with respect to the isophoric array shown in Figure 5a.

The patch antenna array has been designed through CST on a FR4 substrate having a relative permittivity equal to 4.4 at an operating frequency equal to 2.5 GHz. All patch antennas have been fed by a 50 Ω coaxial cable from the back side of the substrate, and the elements' excitation and location have been chosen by using as reference a continuous aperture source identical to the one used in Section 4.3. Finally, in order to satisfy the impedance matching, the location of the feeding point has been optimized at 5.1 mm from the bottom side of the patch antenna.
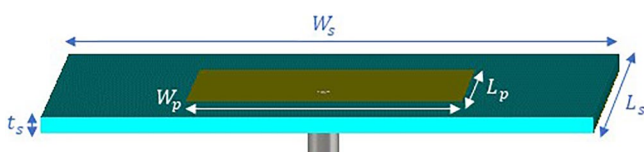
The full-wave electromagnetic simulation of the array generated the power pattern depicted in Figure 9 [where subplots (a) and (b) respectively show the 3-D view and the 1-D main cut through boresight].

Interestingly, Figure 9b also reports the superposition between the power pattern achieved through the full-wave simulation and the one reported in Figure 5b. Notably, although the full-wave simulated antenna allows a

Figure 7. Single patch antenna: design through the CST software as in Wei et al. (2015) and Table 4.

Table 4
Antenna Design Parameters Referring to Figure 7

Parameters symbols	Parameters details	Value (mm)
W_p	Width of patch	36.5
L_p	Length of patch	27.4
W_s	Width of substrate	73
L_s	Length of substrate	54.8
t_s	Height of substrate	1.6

reduction in the number of elements (which drops from 206 to 187), such comparison essentially reveals no significant loss in terms of any radiation parameters. This circumstance confirms not only the high performance of the full-wave simulated array but also, and more importantly, the actual applicability of the given theory to the design of realistic antennas.

5. Conclusions

A new approach to the synthesis of power patterns for target-localization applications has been presented. The technique pursues the generation of a single isolated null of the pattern at the target direction as well as the maximization of the field slope in such direction by exploiting the OAM beam modes. In particular, the most suitable OAM vortex is first identified and, then, the SVD of the corresponding operator followed by a smart CP optimization allows maximizing the localization accuracy while keeping under control both the beamwidth and the sidelobe level of the power pattern. By so doing, the proposed synthesis procedure removes some important limitations of the state-of-the-art OAM-based radars and definitively increases their performance.

The presented method is also very general. In fact, by relying on the optimal synthesis of the continuous aperture field distribution, it results applicable to whatever kind of practical antenna array. The only condition to be fulfilled in order to guarantee high radiation performances is that the adopted array layout allows performing a sufficiently-fine sampling of the continuous reference source, on the one hand, while still avoiding too small inter-element spacing (and hence possible antenna-interference issues), on the other hand (Hodges & Rahmat-Samii, 1996). Applications to equispaced, reconfigurable, sparse, and isophoric arrays have been given, as well as comparisons with recent contributions, confirming the interest and effectiveness of the presented technique.
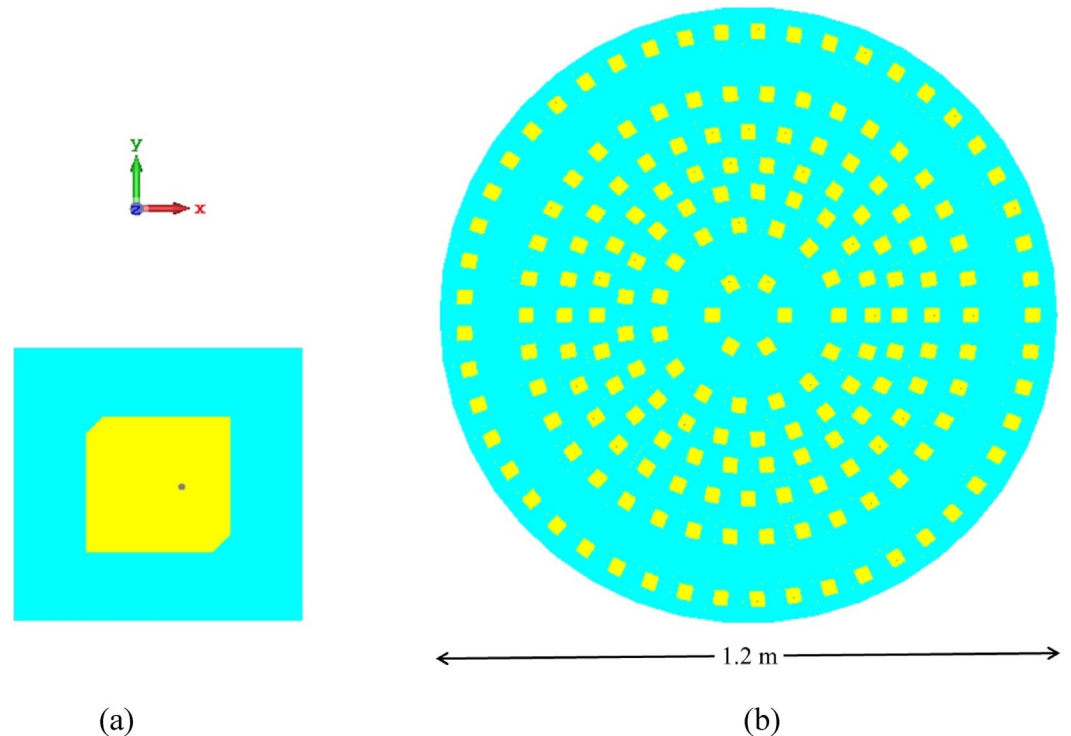

(a)   (b)

Figure 8. Isophoric array CST design by using the antenna shown in Figure 7 as single radiating element: corner truncation which ensures the circular polarization of the antenna—see also (Mekki et al., 2020) [subplot (a)]; overall layout [subplot (b)].
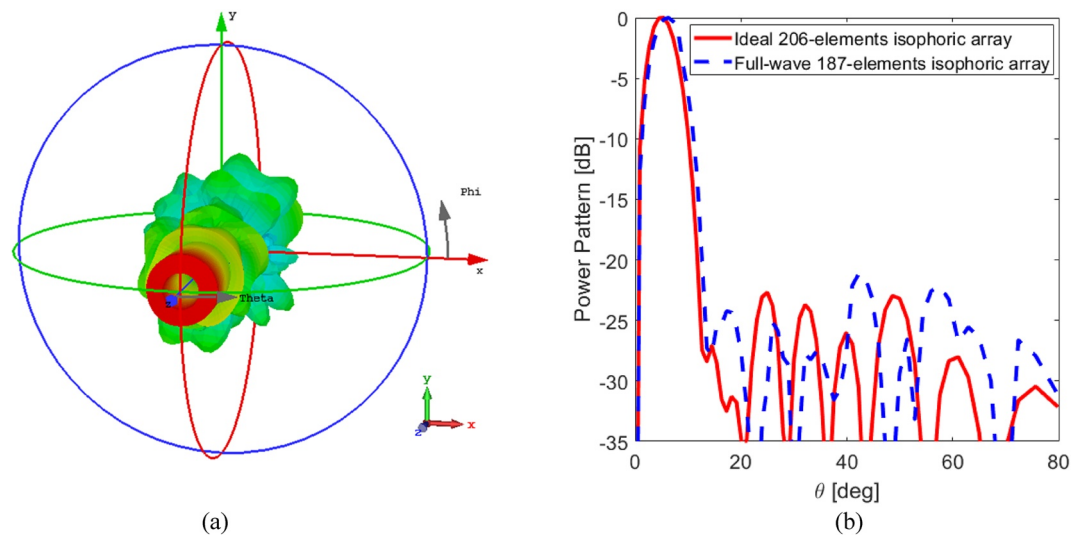
Figure 9. Power pattern achieved through the CST full-wave simulation of the array shown Figure 8: 3-D view [subplot (a)]; 1-D main cut as compared to the solution reported in Section 4.3 [subplot (b)].

Data Availability Statement

All data and software are available at Battaglia et al. (2022).

References

Battaglia, G. M., Isernia, T., Palmeri, R., & Morabito, A. F. (2022). Synthesis of orbital angular momentum antennas for target localization. *Zenodo*. https://doi.org/10.5281/zenodo.7408725

Bayliss, E. T. (1968). Design of monopulse antenna difference patterns with low sidelobes. *Bell System Technical Journal*, *47*(5), 623–650. https://doi.org/10.1002/j.1538-7305.1968.tb00056.x

Bleakney, W. M. (1984). *Airborne missile guidance system*. United States Patent US4442431A.

Bracewell, R. N. (1999). *The Fourier transform & its applications* (pp. 335–340). McGraw-Hill Publishing Company.

Bucci, O., D'Urso, M., & Isernia, T. (2005). Optimal synthesis of difference patterns subject to arbitrary sidelobe bounds by using arbitrary array antennas. *IEE Proceedings - Microwaves, Antennas and Propagation*, *152*(3), 129. https://doi.org/10.1049/ip-map:20045073

Bucci, O., Gennarelli, C., & Savarese, C. (1998). Representation of electromagnetic fields over arbitrary surfaces by a finite and nonredundant number of samples. *IEEE Transactions on Antennas and Propagation*, *46*(3), 351–359. https://doi.org/10.1109/8.662654

Bucci, O., Isernia, T., & Morabito, A. F. (2009). Optimal synthesis of directivity constrained pencil beams by means of circularly symmetric aperture fields. *IEEE Antennas and Wireless Propagation Letters*, *8*, 1386–1389. https://doi.org/10.1109/lawp.2009.2039189

Bucci, O. M., Isernia, T., & Morabito, A. F. (2013). An effective deterministic procedure for the synthesis of shaped beams by means of uniform-amplitude linear sparse arrays. *IEEE Transactions on Antennas and Propagation*, *61*(1), 169–175. https://doi.org/10.1109/tap.2012.2219844

Chen, R., Zhou, H., Moretti, M., Wang, X., & Li, J. (2020). Orbital angular momentum waves: Generation, detection, and emerging applications. *IEEE Communications Surveys & Tutorials*, *22*(2), 840–868. https://doi.org/10.1109/comst.2019.2952453

CST Studio Suite 3D EM simulation and analysis software. (2022). CST Studio Suite 3D EM simulation and analysis software [Software]. 3DS. Retrieved from https://www.3ds.com/products-services/simulia/products/cst-studio-suite

Elliott, R. (1976). Design of line source antennas for difference patterns with sidelobes of individually arbitrary heights. *IEEE Transactions on Antennas and Propagation*, *24*(3), 310–316. https://doi.org/10.1109/tap.1976.1141343

Fan, X., Liang, J., Jing, Y., So, H. C., Geng, Q., & Zhao, X. (2022). Sum/difference pattern synthesis with dynamic range ratio control for arbitrary arrays. *IEEE Transactions on Antennas and Propagation*, *70*(3), 1940–1953. https://doi.org/10.1109/tap.2021.3119107

Fan, X., Liang, J., Zhao, X., Zhang, Y., & So, H. C. (2020). Optimal synthesis of sum and difference beam patterns with a common weight vector for symmetric and asymmetric antenna arrays. *IEEE Transactions on Antennas and Propagation*, *68*(10), 6982–6996. https://doi.org/10.1109/tap.2020.2992860

Hodges, R., & Rahmat-Samii, Y. (1996). On sampling continuous aperture distributions for discrete planar arrays. *IEEE Transactions on Antennas and Propagation*, *44*(11), 1499–1508. https://doi.org/10.1109/8.542075

Kennedy, T. A., Landau, M. I., & Nussbaum, H. (1995). *Combined SAR monopulse and inverse monopulse weapon guidance*. European Patent EP0709691A1.

Kou, N., & Yu, S. (2022). Low sidelobe orbital angular momentum vortex beams based on modified bayliss synthesis Method for Circular Array. *IEEE Antennas and Wireless Propagation Letters*, *21*(5), 968–972. https://doi.org/10.1109/lawp.2022.3153392

Li, M., Liu, Y., & Guo, Y. J. (2021). Design of sum and difference patterns by optimizing element rotations and positions for linear dipole array. *IEEE Transactions on Antennas and Propagation*, *69*(5), 3027–3032. https://doi.org/10.1109/tap.2020.3037764

Li, Q., Li, X., Qi, Z., Zhu, H., Huang, Y., Akram, Z., & Jiang, X. (2019). Pattern synthesis of the multimode orbital angular momentum beams based on the fruit fly optimization algorithm. *International Journal of RF and Microwave Computer-Aided Engineering*, *29*(10). https://doi.org/10.1002/mmce.21876

Li, Q., Qi, Z., Huang, Y., Zhu, H., Li, X., Li, X., & Jiang, X. (2018). Orbital angular momentum beams synthesis based on the fruit fly optimization algorithm. In *2018 IEEE Asia-Pacific conference on antennas and Propagation (APCAP)* (pp. 490–491). https://doi.org/10.1109/apcap.2018.8538113

Lin, M., Gao, Y., Liu, P., & Liu, J. (2016). Super-resolution orbital angular momentum based radar targets detection. *Electronics Letters*, *52*(13), 1168–1170. https://doi.org/10.1049/el.2016.0237

Liu, K., Liu, H., Qin, Y., Cheng, Y., Wang, S., Li, X., & Wang, H. (2016). Generation of OAM beams using phased array in the Microwave Band. *IEEE Transactions on Antennas and Propagation*, *64*(9), 3850–3857. https://doi.org/10.1109/tap.2016.2589960

McNamara, D. (1993). Direct synthesis of optimum difference patterns for discrete linear arrays using Zolotarev distributions. *IEE Proceedings H Microwaves, Antennas and Propagation*, *140*(6), 495. https://doi.org/10.1049/ip-h-2.1993.0081

Mekki, K., Necibi, O., Boussetta, C., & Gharsallah, A. (2020). Miniaturization of circularly polarized patch antenna for RFID reader applications. *Engineering, Technology & Applied Science Research*, *10*(3), 5655–5659. https://doi.org/10.48084/etasr.3445

Morabito, A. F., Di Donato, L., & Isernia, T. (2018). Orbital angular momentum antennas: Understanding actual possibilities through the aperture antennas theory. *IEEE Antennas and Propagation Magazine*, *60*(2), 59–67. https://doi.org/10.1109/map.2018.2796445

Morabito, A. F., Isernia, T., & D'Urso, M. (2010). Synthesis of difference patterns via uniform amplitude sparse arrays. *Electronics Letters*, *46*(8), 554–556. https://doi.org/10.1049/el.2010.3591

Morabito, A. F., & Nicolaci, P. G. (2018). Circular-ring antenna arrays being at the same time sparse, isophoric, and phase-only reconfigurable: Optimal synthesis via continuous aperture sources. *Progress in Electromagnetics Research M*, *63*, 1–11. https://doi.org/10.2528/pierm17091902

Morabito, A. F., Palmeri, R., Morabito, V. A., Laganà, A. R., & Isernia, T. (2019). Single-surface phaseless characterization of antennas via hierarchically ordered optimizations. *IEEE Transactions on Antennas and Propagation*, *67*(1), 461–474. https://doi.org/10.1109/tap.2018.2877270

Morabito, A. F., & Rocca, P. (2010). Optimal synthesis of sum and difference patterns with arbitrary sidelobes subject to common excitations constraints. *IEEE Antennas and Wireless Propagation Letters*, *9*, 623–626. https://doi.org/10.1109/lawp.2010.2053832

Palmeri, R., Battaglia, G. M., Morabito, A. F., & Isernia, T. (2022). Reflector antennas characterization and diagnostics using a single set of far-field phaseless data and crosswords-like processing. *IEEE Transactions on Antennas and Propagation*, *70*(9), 8424–8439. https://doi.org/10.1109/tap.2022.3168652

Palmeri, R., Bevacqua, M. T., Morabito, A. F., & Isernia, T. (2018). Design of artificial-material-based antennas using inverse scattering techniques. *IEEE Transactions on Antennas and Propagation*, *66*(12), 7076–7090. https://doi.org/10.1109/tap.2018.2871707

Piessens, R. (2000). The Hankel transform. In A. D. Poularikas (Ed.), *The transforms and applications handbook 2000 (Electrical engineering handbook)* (2nd ed.). CRC Press.

Qi, Y. X., & Li, J. Y. (2021). Difference pattern synthesis based on superposition principle. *IEEE Transactions on Antennas and Propagation*, *69*(5), 3005–3009. https://doi.org/10.1109/tap.2020.3025213

Qin, Y., Liu, K., Cheng, Y., Li, X., Wang, H., & Gao, Y. (2017). Sidelobe suppression and beam collimation in the generation of vortex electromagnetic waves for radar imaging. *IEEE Antennas and Wireless Propagation Letters*, *16*, 1289–1292. https://doi.org/10.1109/lawp.2016.2633008

Wei, W., Mahdjoubi, K., Brousseau, C., & Emile, O. (2015). Generation of OAM waves with circular phase shifter and array of patch antennas. *Electronics Letters*, *51*(6), 442–443. https://doi.org/10.1049/el.2014.4425

Yin, X., Hao, J., Han, J., Xu, C., Xin, X., Li, L., & Yu, C. (2014). Sidelobe suppression in the generation of beam carrying orbital angular momentum. In *2014 13th international conference on optical communications and networks (ICOCN)*. https://doi.org/10.1109/icocn.2014.6987108

Yu, S., & Kou, N. (2023). Synthesis for OAM vortex electromagnetic waves based on Fourier-Bessel expansion. *IEEE Transactions on Antennas and Propagation*, *71*(2), 1539–1547. https://doi.org/10.1109/tap.2022.3225587

Zhang, C., & Chen, D. (2017). Large-scale orbital angular momentum radar pulse generation with rotational antenna. *IEEE Antennas and Wireless Propagation Letters*, *16*, 2316–2319. https://doi.org/10.1109/lawp.2017.2716408

Zhang, C., Jiang, X., & Chen, D. (2019). RCS promotion in orbital angular momentum imaging radar with rotational antenna. *IET Radar, Sonar & Navigation*, *13*(12), 2140–2144. https://doi.org/10.1049/iet-rsn.2019.0100

Zhu, Z., Zheng, S., Xiong, X., Chen, Y., Hui, X., Jin, X., et al. (2022). A non-uniform travelling-wave current source model for designing OAM Antenna: Theory, analysis and application. *IEEE Access*, *10*, 47499–47508. https://doi.org/10.1109/access.2022.3170713